Living Optical Random Neural Network with Three Dimensional Tumor Spheroids for Cancer Morphodynamics: Supplementary Information

D. Pierangeli,[1,2] V. Palmieri,[3,4] G. Marcucci,[1,2] C. Moriconi,[5]
G. Perini,[3,4] M. De Spirito,[3,4] M. Papi,[3,4] and C. Conti[1,2]

[1] *Institute for Complex Systems, National Research Council (ISC-CNR), 00185 Rome (IT)*
[2] *Department of Physics, University Sapienza, 00185 Rome (IT)*
[3] *Fondazione Policlinico Universitario A. Gemelli, IRCCS, 00168 Rome (IT)*
[4] *Institute of Physics, Università Cattolica del Sacro Cuore, 00168 Rome (IT)*
[5] *School of Pharmacy and Pharmaceutical Sciences, Cardiff University, CF10 3NB Cardiff (UK)*

SUPPLEMENTARY NOTE 1: PROPAGATOR AND GREEN'S FUNCTION FORMALISM, REVIEW OF LIGHT PROPAGATION IN RANDOM MEDIA AND LINK WITH RANDOM NEURAL NETWORKS

We first review the Green function formalism[1] [2–4], which shows the way light propagation in a complex medium is mapped to a neural network (NN) model.

We follow [3], and adopt the Dirac notation formalism which is handy for classical vectorial waves. This notation is detailed in the book by Economou [2]. The field scattered by a random medium is $|\mathbf{E}\rangle = \mathbf{K}|\mathbf{E}^{\text{in}}\rangle$, where $|\mathbf{E}^{\text{in}}\rangle$ is the incident field and $\mathbf{K} = \mathbf{1} - \mathbf{G}\mathbf{e}_s$ is a generalized propagator, [5] $\mathbf{1}$ is the identity operator, and the Green function $\mathbf{G}$ is such that

$$(\boldsymbol{\mathcal{D}} + \mathbf{e})\,\mathbf{G} = \mathbf{1}. \tag{1}$$

In equation (1), $\boldsymbol{\mathcal{D}}(\mathbf{r}) = -\nabla \times \nabla\times$, and $\mathbf{e} = \mathbf{e}_b + \mathbf{e}_s$ is the operator given in terms of the position representation

$$\langle \mathbf{r}|\mathbf{e}|\mathbf{r}'\rangle = k_0^2 \varepsilon(\mathbf{r})\delta(\mathbf{r} - \mathbf{r}') \tag{2}$$

associated to the relative permittivity $\varepsilon(\mathbf{r}) = \varepsilon_b(\mathbf{r}) + \varepsilon_s(\mathbf{r})$, where $\varepsilon_b(\mathbf{r}) = 1$ is the permittivity of the homogenous background medium and $1 + \varepsilon_s(\mathbf{r})$ is the relative permittivity of the scattering medium.

In the position representation, $\mathbf{r}$ the propagator reads

$$\langle \mathbf{r}|\mathbf{K}|\mathbf{r}'\rangle = \delta(\mathbf{r} - \mathbf{r}') - k_0^2 \varepsilon(\mathbf{r}')\langle \mathbf{r}|\mathbf{G}|\mathbf{r}'\rangle, \tag{3}$$

and its matrix elements are

$$k_{mn} = \langle m|\mathbf{K}|n\rangle, \tag{4}$$

where $|n\rangle$ corresponds to input/output eigenmodes, or "channels", as detailed in [3].

Transmission through disordered media as a random NN layer

Given the input field $|\mathbf{E}^{\text{in}}\rangle$, one can choose a basis representation, such that the input is represented by a vector E_n^{in} with $n = 1, ..., N$. As the input SLM is set in the Fourier input plane, each n is a different plane wave corresponding to each segment in the SLM. The SLM pixels are grouped in a number N of segments and, as also detailed below, the SLM and the related Fourier-transforming optics act as an optical convolutional NN layer. As the total field in the presence of the scatterer is $|\mathbf{E}\rangle = \mathbf{K}|\mathbf{E}^{\text{in}}\rangle$, one can represent the trasmission through the system by the matrix elements k_{mn}, such that letting $E_n = \langle n|\mathbf{E}\rangle$

$$E_m = \sum_{n=1}^{N} k_{mn} E_n^{\text{in}} \tag{5}$$

Equation (5) can be represented as in Supplementary Figure 1a: to the input mode with amplitude E_n^{in} is associated the input node n, for the output node with amplitude E_m we have the output node m and the link is weighted by the coefficient k_{mn}. A schematic representation of the overall network is in in Supplementary Figure 1b, with $\mathbf{x}$ denoting the input vector with components $x_n = E_n^{\text{in}}$ and $n = 1, 2, ..., N$; $\mathbf{y}$ is the output vectors, with components $y_n = E_n$ and $n = 1, 2, ..., N$.

The effect of the perturbations by external stimuli

In the presence of the perturbation, the perturbed propagator is

$$\mathbf{K}' = \mathbf{1} - \mathbf{G}'\mathbf{e}' \tag{6}$$

with $\mathbf{G}'$ the perturbed Green's function such that

$$(\boldsymbol{\mathcal{D}} + \mathbf{e}_b + \mathbf{e}_s + \mathbf{e}')\,\mathbf{G}' = \mathbf{1}, \tag{7}$$

and $\mathbf{e}'$ is the operator associated to the perturbed permittivity $\Delta\varepsilon(\mathbf{r})$, where $\varepsilon(\mathbf{r}) = \varepsilon_b(\mathbf{r}) + \varepsilon_s(\mathbf{r}) + \Delta\varepsilon(\mathbf{r})$ is the total relative permittivity.

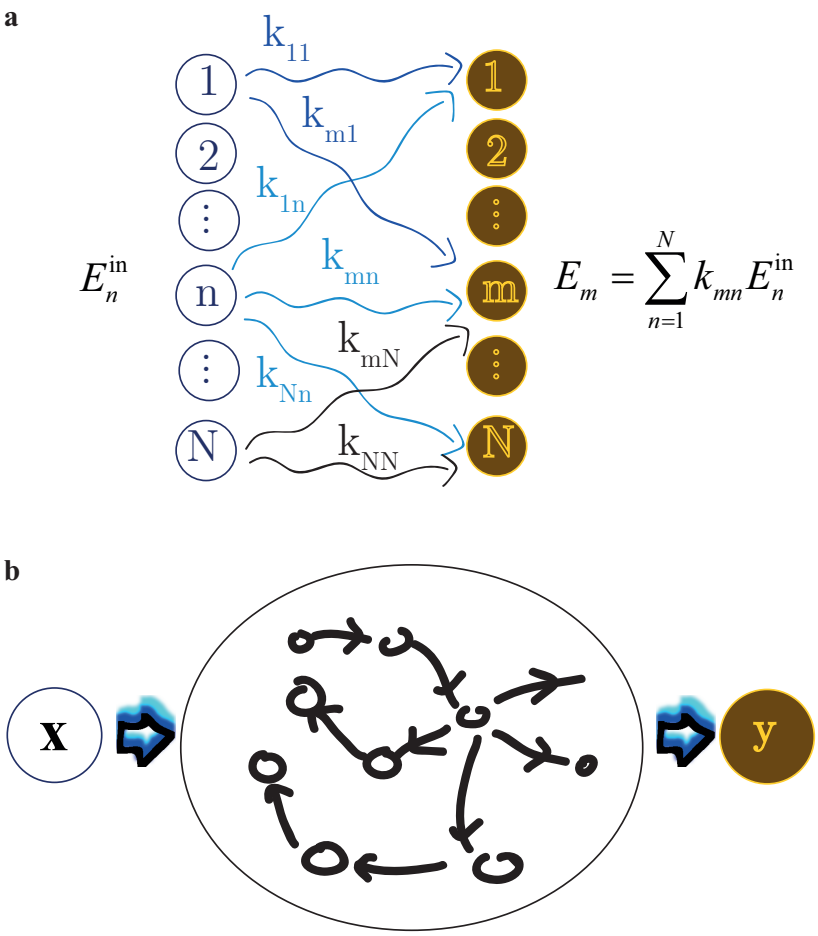

Supplementary Figure 1. Representing light propagation in a random medium as a layer of a neural network with random coefficients. (a) Dense layer representing Eq. 5 in Supplementary Note 1. The components of the electric field $E^{\text{in}}_{1,2,\dots,N}$ are the label sof the inputs. The elements of the trasmission matrix k_{mn} are the weights. The components of the transmitted field E_m are the output labels. (b) Representation of the random layer.

The field in the presence of perturbation $|\mathbf{E}'\rangle$ can be then expressed in terms of the state without perturbation $|\mathbf{E}\rangle$ and the input state $|\mathbf{E}^{\text{in}}\rangle$ as operator multiplication

$$|\mathbf{E}'\rangle = \mathbf{K}'|\mathbf{E}\rangle = \mathbf{K}'\mathbf{K}|\mathbf{E}^{\text{in}}\rangle. \tag{8}$$

Correspondingly, the transmission matrix elements k^{P}_{mn} in the presence of the nonlinear perturbation is written as a matrix multiplication

$$k^{(\text{P})}_{mn} = \sum_{q=1}^{N} k'_{mq} k_{qn}. \tag{9}$$

To simplify the notation, we omit in the following the sum over repeated indices, and Eq. (9) reads

$$k^{(\text{P})}_{mn} = k'_{mq} k_{qn}. \tag{10}$$

In addition, we introduce a tensorial notation by using a three index tensor k_{mnq}, such that

$$k_{mn1} = k_{mn}, \tag{11}$$

, and

$$k_{mn2} = k^{(P)}_{mn} \tag{12}$$

. This notation is useful when one has many layers, and each layer corresponds to a different value of the third index q. In this notation, Eq. (9) reads

$$k_{mn2} = k'_{mq} k_{qn1}. \tag{13}$$

By using (6), the element of the rotation matrix k'_{mq} is written as

$$k'_{mq} = \delta_{mq} + w_{mq}, \tag{14}$$

with δ_{mq} the Kronecker symbol and the perturbation elements

$$w_{mq} = -\langle m|\mathbf{G}'\mathbf{e}'|q\rangle. \tag{15}$$

The element of the perturbed matrix can then be written as

$$k_{mn2} = k_{mn1} + w_{mq} k_{qn1} = k_{mn1} + w_{m1} k_{1n1} + ... + w_{mN} k_{Nn1}. \tag{16}$$

Eq. (16) is graphically represented in Supplementary Figure 2, and can be interpreted as follows: in the absence of perturbation, light is channelled - with amplitude k_{mn} - from the channel n to the channel m, see Supplementary Figure 2a. In the presence of the perturbation, further contributions arise from other channels. For example, the light channeled from n to 1 with amplitude k_{1n} also contributes to the signal in the channel m with amplitude w_{1m}, see Supplementary Figure 2b.

This may be described by stating that any perturbation add further channels for light by scattering from one unperturbed channel to another or, in terms of NNs, this corresponds to a new layer whose weights w_{mn} are proportional to the strength of the perturbation. This is sketched in Supplementary Figure 3: in the presence of the perturbation, the input signal $\mathbf{x}$ activates an hidden layer with state vector $\mathbf{h}^{(1)}$ and elements h_{m1}, such that

$$h_{m1} = k_{mn1} x_n; \tag{17}$$

and the hidden layer activate the output layer as

$$y_m = k'_{mq} h_{q1} = k'_{mq} k_{qn1} x_n = k_{mn2} x_n. \tag{18}$$

SUPPLEMENTARY NOTE 2: LAYERS OF THE RANDOM OPTICAL MACHINE

We detail in the following the internal architecture of the random optical machine (ROM).

The layers

Following the main manuscript, the scheme of the "training configuration" is detailed in the Supplementary Figure 4. The beam amplitudes at the SLM segments A_i are the inputs, and the cost function is obtained by the output of a convolutional layer applied to the average intensities y_i at the CCD segments. We detail in the following the different layers.

- The SLM and the optical setup form an optical convolutional layer.

  In a convolutional layer, a sliding window filter scans an input image to extract a number of output segments smaller than the number of pixels. According to the number of pixels and adopted segments the input $N \times M$ maps is convoluted with a $K \times K$ filter. [6] The number of segments, and correspondingly the size of the pooling filter is a hyperparameter of the network.

  In our optical setup, The SLM is located in the Fourier plane, and spatially samples the Fourier transform of the laser beam $E(x, y)$, denoted as $\tilde{E}(k_x, k_y)$, into a matrix of pixels 1024×768. The matrix is divided into segments forming a smaller matrix with size 72×72. The light intensity at the ij SLM segment is A_{ij}. The set of the A_{ij} is the input to the direct network. In the following, we use a single index for the matrix elements to simplify the notation A_n.

  For each segment, the SLM action is mathematically described by a transfer function $H_n(k_x, k_y)$, which is a window with the size of the segment n and zero outside.

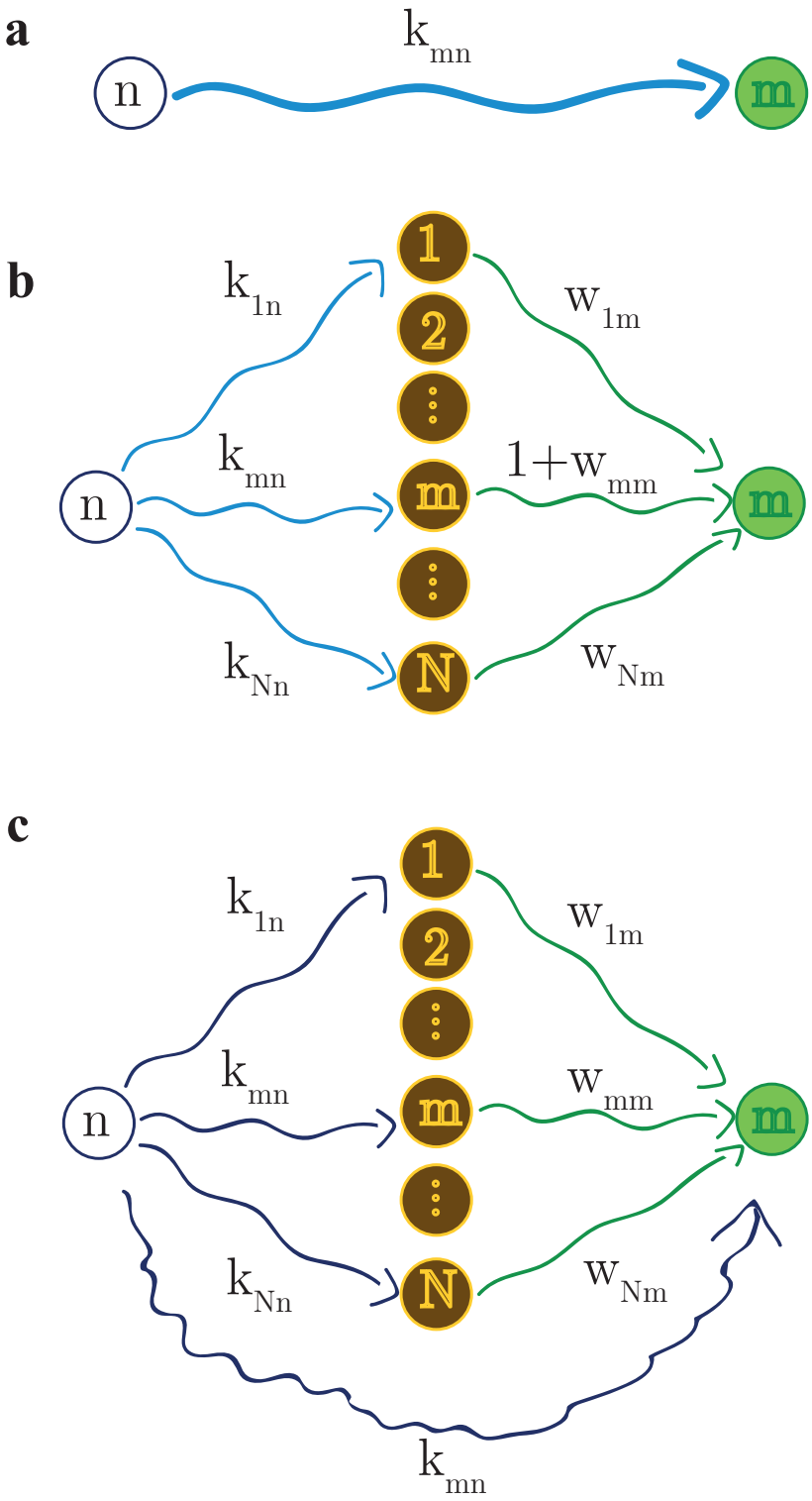

Supplementary Figure 2. Schematics of the effect of the perturbation in the artificial neural network. (a) Unperturbed transmission linking input channel n, and the output channel m. (b) In the presence of the perturbation, new links are created and all the channel in addition to the channel n contribute to the output m, see Eq. (18) in Supplementary Note 1. (c) As in (b) an equivalent representation of Eq. (18) in Supplementary Note 1. Note that the internal layer indeces (gold) refer to the hidden state variable $\mathbf{h}^{(1)}$. k_{mn} are the weights corresponding to the components of the unperturbed transmission matrix. w_{mn} are the weights due to the nonlinear perturbation as in Eq.15 of the Supplementary Note 1.

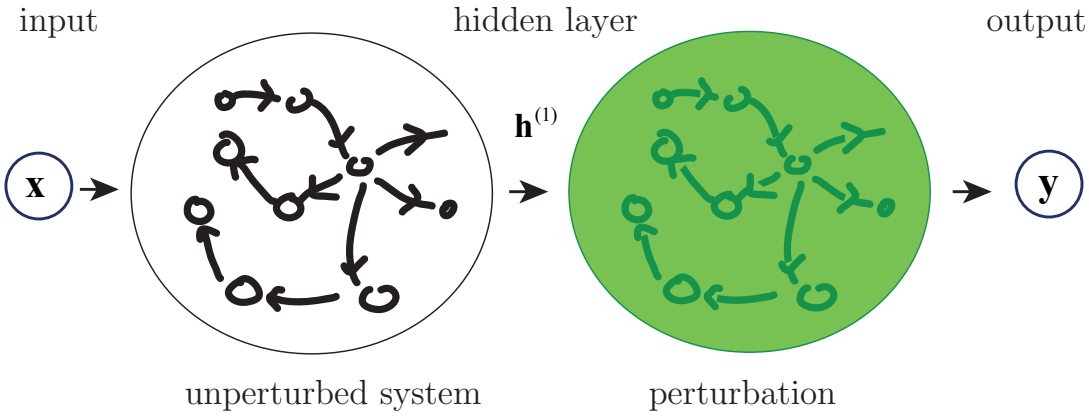

Supplementary Figure 3. Synthetic representation of the effect of any perturbation to the input and output vector, through the formation of a hidden layer, with state vector $\mathbf{h}^{(1)}$.

For a phase-modulation SLM, H_n includes a phase shift w_n.

After the SLM the fields propagate to the sample and is again Fourier transformed by optical propagation and the imaging system we use (lenses, microscope objective, see the setup in Fig. 2 of the main manuscript). The overall optical setup hence realizes a convolution, with a set of weights w_n and hyperparameters given by the size and the number of the segments of the SLM (in our case this is chosen to be 72×72).

In the corresponding mathematical model of the NN, the action of the SLM layer on the input vector A_n is furnishing an output value (within an inessential multiplicative factor due to the attenuation of the beam in the optical setup)

$$h_m^{(1)} = A_n e^{\imath w_n} \tag{19}$$

- Transmission in the random medium as **deep reservoir computing**.

In reservoir computing (RC), a large part of the network is left untrained and random, and training occurs only at the input and the readout. Various paradigms have been developed and applied, also in the field of photonics. RC has the strategic advantage of avoiding training entire huge networks, and can be implemented with random media.

In very recent years, the paradigm of "**deep reservoir computing**", is emerging. Examples include the so-called deep state networks, and related investigations. [7, 8] Notably, this deep architecture may also have linear layers in the presence of unidirectional flow. [9]

As discussed above the transmission through the random medium is described by a random matrix. Any perturbation adds a further internal layer in the reservoir.

In our case, we have two parameters; one is the pump of the IR laser beam and the other is the amount of chemotherapy. We do not train the deep internal layers of the reservoir, but switch them on/off by controlling the external stimuli.

We also remark that the fact that the flow of information is unidirectional qualifies this as a "deep convolutional layer." Indeed some channels are lost because of the scattering through the random medium. In other words, inverting information flow, does not produce the same input, as the channels retained output (those included in the numerical aperture of the collecting optics) does not contain all the input light.

- CCD camera as an electronic convolutional NN pooling layer.

The optical field is imaged in the CCD camera, which returns a matrix with size 1280×1024. The CCD camera makes the modulus square of the field, hence performs a nonlinear operation. Then we use a **pooling layer**, which is a special class of convolutional NNs, and map the CCD image into 72×72. Each element of the reduced matrix is an average of the number of the CCD matrix pixels entering the CCD segment. The output of this layer is a vector $\mathbf{g}$ with length equal to the number of the CCD segments.

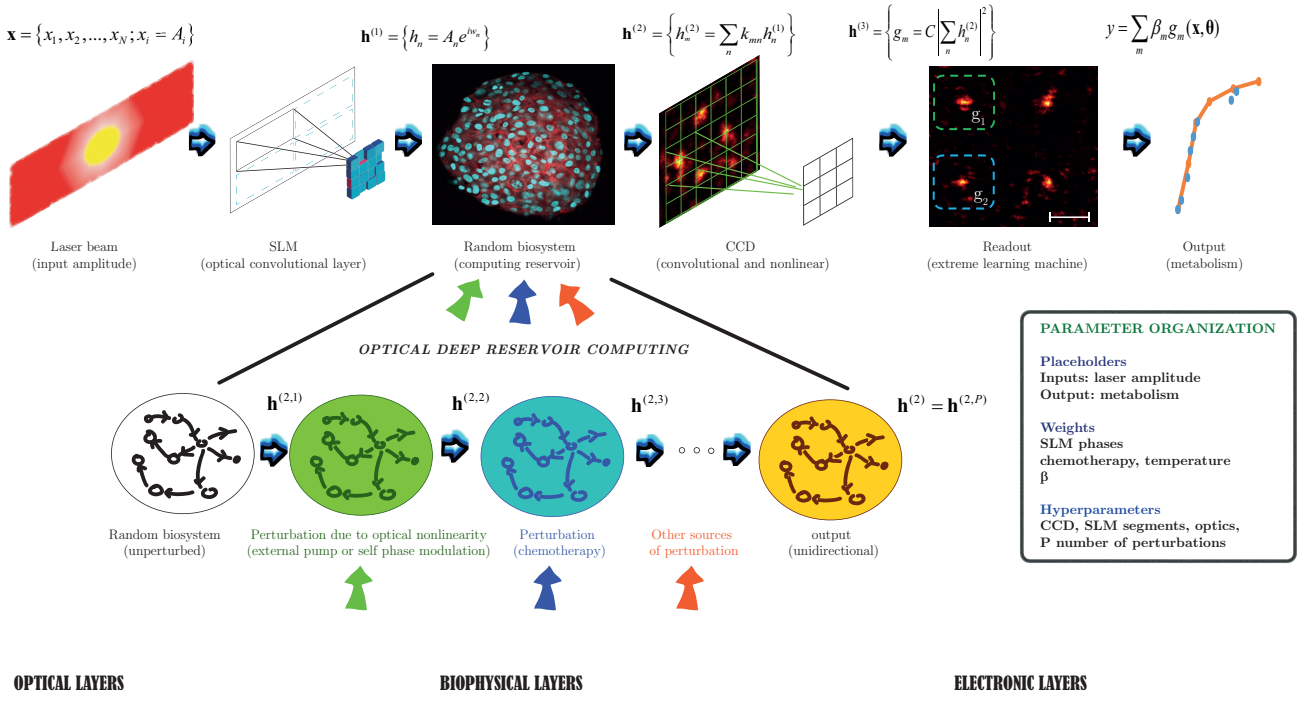

Supplementary Figure 4. Schematics of the Random Optical Machine (ROM) in the training configurations. The various parameters are optimized to retrieve as output a specific biophysical quantity (e.g., the metabolism), validated by conventional optical techniques. The optical layers are formed by the laser beam (input) and the spatial light modulator (optical convolutional layer). The 3D Tumor Model (3DTM) is the biophysical random computing reservoir. The Charge-Coupled Device (CCD) camera acts as an electronic pooling layer and the Extreme Learning Machine (ELM) readout converts the signal in relevant measurements, as the response time and the metabolism. The corresponding mathematical expressions of the ROM states are also indicated. The network can be continuously retrained to follow the dynamics of the 3DTM on slow time scales. In the bottom panels, external perturbations on the 3DTM, such as infrared (IR) laser pumping and chemotherapy, introduce further random layers and change the computing reservoir.

- Readout layer and the **extreme learning machine**.
  The readout layer is made by software and has output a combination of the intensity at the CCD segments g_i.

$$y = \sum_m \beta_m g_m(\mathbf{x}) \tag{20}$$

  The coefficients of the combination β_m fix the number of the output layers as in the "extreme learning machine". In the extreme learning machine, the number of output is trained to achieve a given functionality. [10] In the case we need a single input at the segment m, we fix $\beta_n = 0$ for $n \neq m$. For optimizing two or more spots, we set the two corresponding β_s as different from zero.

- Cost function.
  For a single spot target, we maximize $f = y_1^2$, for two spots we maximize $f = (\beta_1 y_1 + \beta_1 y_2)^2$, and so on.

Validation of the trained ROM by comparison with conventional optical techniques

Once the network is trained, the transmitted light is maximized and this directly provides information on metabolism and other physical properties.

We use the network to retrieve information about the thermal response and the effect of chemotherapy. As detailed in the main manuscript, the thermal response is specifically relevant for applications in tumour treatments by hyperthermia, and to determine the thermo-responsivity of cells. The chemotherapy response is critical for assessing the minimal drug amount, which is effective on 3DTM metabolism. Supplementary Figure 5 shows the inverse configuration for the ROM, with details on the parameter organization.

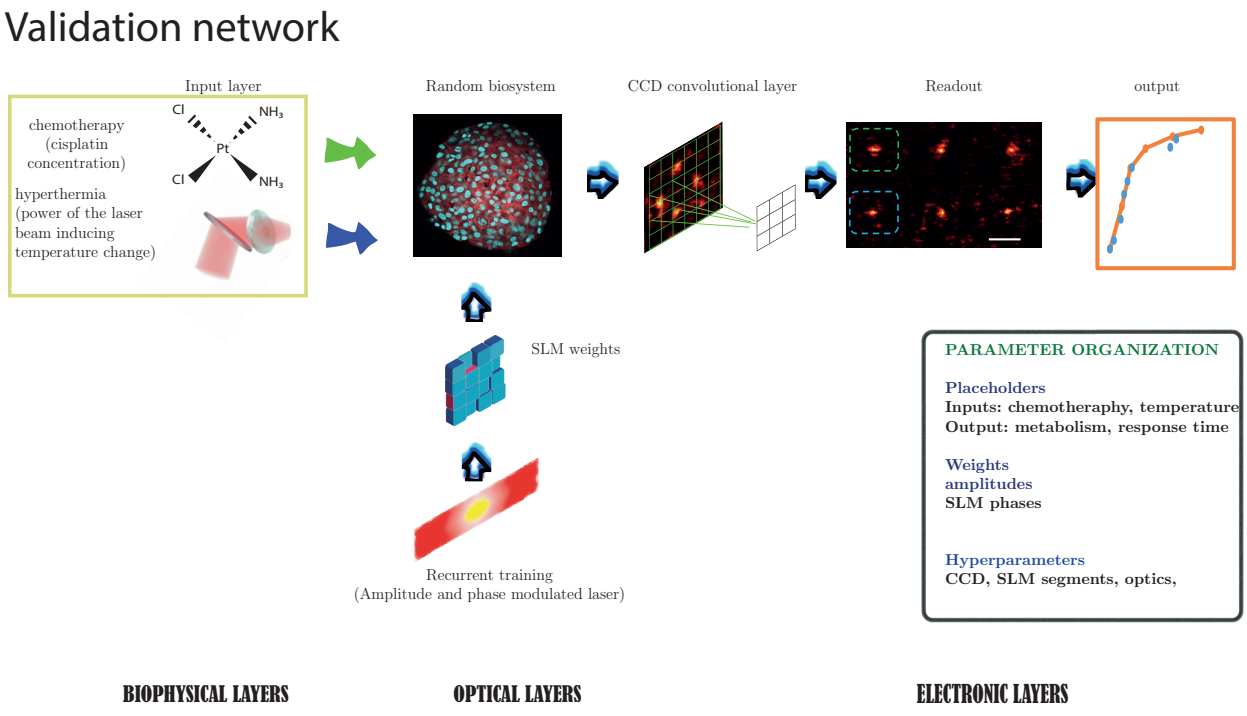

Supplementary Figure 5. Schematics of the artificial neural network in the validation configuration. The input of the network is the perturbation, as the amount of chemotherapy or the power for laser heating. The network furnishes information on the way this input affect the metabolism; for example, to assess the role of the chemotherapy on the tumor growth. The internal part of the network is the tumor model, the Spatial Light Modulator phase profile (SLM weights), and the laser. This is followed by the detection, formed by the Charge-Coupled Device (CCD), the pooling of the CCD image into section, and the readout, which perfomrs a weighted sum of the output channels. The inset describes the role of the various parameters of the network,the placeholders are input and output, the weights are the SLM and laser parameters. The hyperparameters are optimized to improve the response of the systems.

As inputs, one has the temperature and the chemotherapy (detailed below), the output here correspond to single focus-spot, which is enough to retrieve information about the thermal response. More complex output functions may be conceived, for example, to discriminate heterogeneity in the 3DTM evolution and response, which will be considered in future work.

By comparison with conventional optical imaging (COI), we show in the main manuscript that the ROM retrieves the thermal response time and the metabolisms in a way that outperforms COI.

We report in the following more details on the measurement of the thermal response and of the metabolism.

SUPPLEMENTARY NOTE 3: ROM DETECTION OF LASER-INDUCED HYPERTHERMIA: EXTENDED RESULTS

Additional results when the tumour spheroid is perturbed with the infrared pump laser to induce hyperthermia are reported in Supplementary Figure 6. Infrared laser-induced temperature variations in brain tissue are very relevant for many applications, as imaging and cancer studies. According to the literature,(refs. 29-31 of the main manuscript) a temperature variation of the order of 10° C induces irreversible changes. We hence limit our IR pump laser power inside the cell (i.e., after reflection of the pump lasers by the sample container and input optics) to the order of 0.1 W, for time intervals of the order of 1000 s, which corresponds to a total irradiation energy of maximum 100 J, which transferred to a 1 cm^3 of water containing the glioblastoma spheroid induces a temperature variation of the order of 10° C. The evolution of the output single-point target as the cancer spheroid changes morphology over time is shown in Supplementary Figure 6a. Since no recurrent training is present, the bio-photonic machine cannot anymore synthesize the function, and the whole output intensity distribution decorrelates. The machine functionality can be maintained if the recurrent training is active during the morphodynamics. The output distribution detected with this recurrent approach is reported in Supplementary Figure 6b for pump powers (before entering the sample container)

$P = 0.6$ W, respectively. As a result of the adaptive machine process, the intensity in the target is maintained almost constant during the pumping stage. To quantify variations in the output function under pumping for the case with fixed (Supplementary Figure 6a) and continuously-adjusted weights (Supplementary Figure 6c), we compute the statistical overlap between the unperturbed intensity distribution and the evolving ones:

$$\text{overlap}(t) = \frac{\sum_t \sum_y I_0(t) I_t(y)}{\sum_t \left(\sqrt{\sum_y I_0(y)^2}\right) \left(\sqrt{\sum_y I_t(y)^2}\right)}, \tag{21}$$

where $I_t(y)$ is the output intensity $y-$distribution detected at time t. As shown in Supplementary Figure 7d, the transmitted light spatially decorrelates when hyperthermia is induced by the infrared pump beam. However, this decorrelation is partially compensated by the recurrent learning process, which fixes the output function in the proximity of the target area. The overlap decay strongly depends on the intensity of the IR beam. From the minimum of the decorrelation function, we can estimate the typical response time as a function of the pump power (see Fig. 4, main manuscript). We find that the induced morphological change in the cancer spheroid occurs as fast as the power of infrared beam increases. Further experiments are performed also varying the exposure time at fixed powers.

SUPPLEMENTARY NOTE 4: ROM TRACKING OF TUMOUR GROWTH: EXTENDED RESULTS

When living tumour cells are employed as a reservoir of the optical NN, the machine output strongly depends on time through the natural growth of the cancer spheroid. We track the system evolution repeating experiments at different waiting times from the moment in which the tumour spheroid is removed from its growth environment. For the living machine output (recurrent training on) reported in Supplementary Figure 7a. The waiting time is approximately 110 min, and the evolution is tracked for 105 min. We observe that the efficiency of the operation improves, that is, the intensity in the single-point target increases with time. Specifically, we define the time-dependent operation enhancement

$$\eta(t) = \frac{I_{target}(t)}{\langle I_0 \rangle} \tag{22}$$

where $\langle I_0 \rangle$ is the spatially-averaged transmitted intensity before the training. As reported in Supplementary Figure 6b, the enhancement probability distribution function (PDF) changes during the evolution in Supplementary Figure 7a, with the mean value $\bar{\eta}$ sharply passing to a larger value. The same behavior is observed for living cells under the cytotoxic action of the chemotherapeutic drug, as reported in Supplementary Figure 7c for CIS 80 μg/ml pharmacological treatment and waiting time 180 min. In this case, the apoptotic effect of the cisplatin results in an output signal with reduced intensity. We can extract quantitative information on the internal tumour dynamics considering the evolution of η, which reflects the interplay between changes occurring in the reservoir and recurrent learning of the machine. The enhancement predicted at large N for our approach is (Ref. 22, main manuscript):

$$\bar{\eta} = \frac{T_P}{2t_{iter}} \tag{23}$$

where t_{iter} is the algorithm iteration time ($t_{iter} = 0.22$ s in our experiment) and T_P is the so-called persistence time, here indicating the typical time scale on which variations of the disordered 3D cell structure occur. For living spheroids, it signals how the internal motion gradually slow down (blue dots in Supplementary Figure 7d) due to the reduced mobility and size growth of the tumour out of its optimal controlled environment. When the chemotherapeutic drug is introduced, the measured persistence time signals a fast cellular death (red dots in Supplementary Figure 7d) that becomes less efficient on time. More importantly, after several hours from the treatment, the internal action of the drug is still detectable.

SUPPLEMENTARY NOTE 5: TRAINING ALGORITHM, DISCUSSION

We describe in the methods of the main manuscript the adopted training algorithm. Alternative strategies may be envisaged. A class of algorithms that is well suited for the present optical implementation, where we train the input layer, is those of genetic algorithms, which have also been exploited for optical pattern recognition. The basic idea when applied to our setting is to create a population of initial phase masks and rank them according to the measured cost function on the output plane. At each iteration, these phase masks are optimized through breeding and mutation

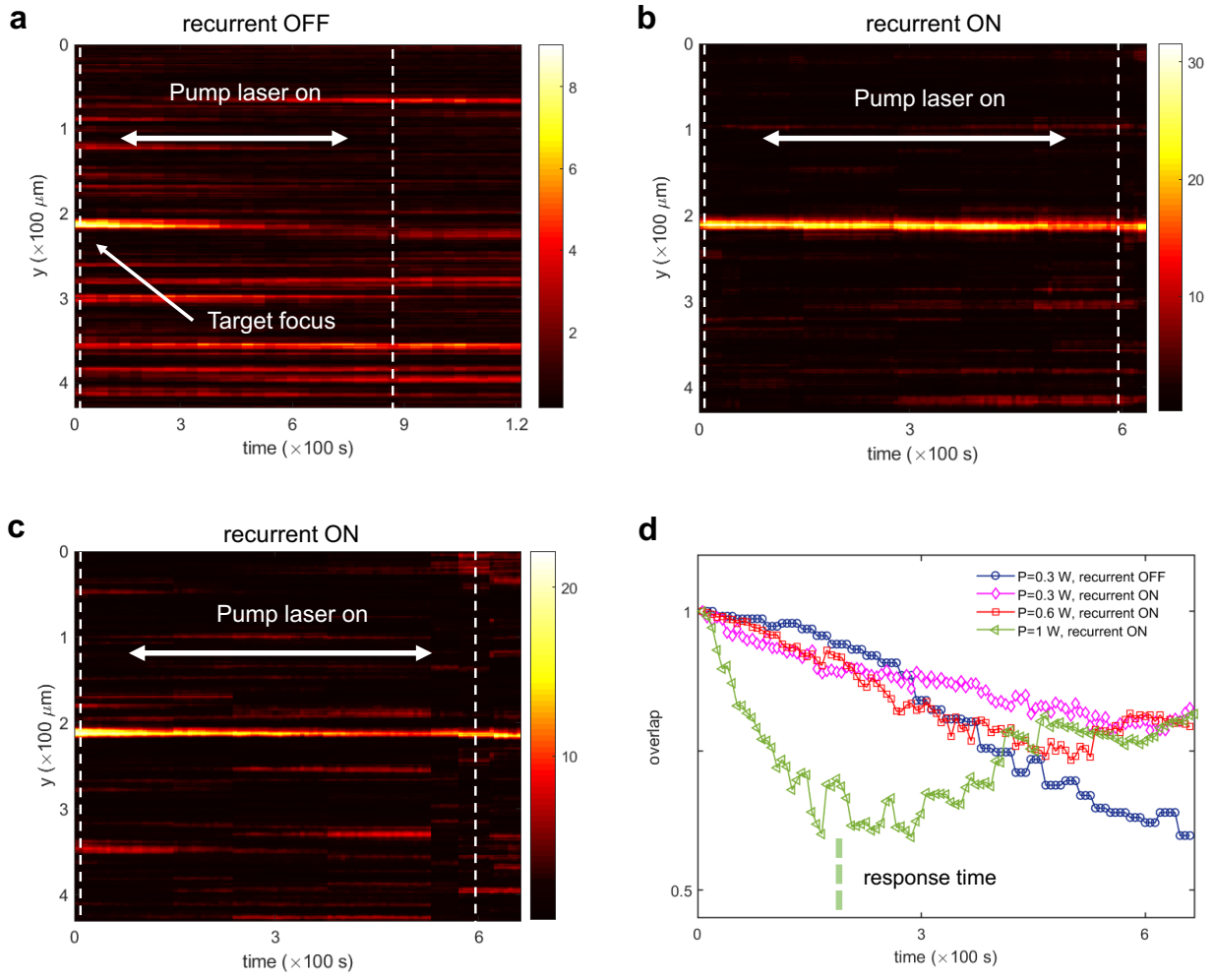

Supplementary Figure 6. Photonic neural network output for tumor spheroids under hyperthermia. Evolution of the machine output under tumour pumping with power P; panels a,b,c show the intensity profile in arbitrary units on the CCD camera pixel in the y-direction versus time : (a) $P = 0.3$ W and (b) $P = 0.6$ W for (a) static input weights and (b,c) recurrent training. (d) Correlation overlap of the whole evolving output intensity distribution for different pump powers. The minimum in the correlation overlap [Eq. (21) of Supplementary Note 4] indicates the response time (see Fig. 4d of the main manuscript).

operations. Specifically, offspring is created by random combinations with random weights; they are ranked and added within the existing population through a generational method until a satisfactory solution is achieved. This kind of algorithm has been proven to be particularly advantageous in low signal-to-noise environments[11]. However, they require an extremely large number of calls to the output plane and, considering that our purpose is not to optimize the efficiency, we prefer a more general approach. Concerning other algorithms that operate sequentially, our training routine has the major advantage of reaching within the lowest possible number of iterations the saturation level in terms of enhancement of the intensity of the output target. More importantly, for a large number of input nodes N, the achievable enhancement depends only on the involved time scales, a fundamental property we exploit to probe the morphodynamics of tumors freely evolving and under chemotherapy. For a fixed spheroid (Fig. 2b of the main manuscript), same realizations of our training routine give an error in terms of enhancement of the single-point target within approximately 10%. Residual amplitude modulation constitutes one of the main sources of noise since it produces unbalanced scattering paths that cannot be completely compensated outside the target region. On the other hand, an amplitude-only modulation system can be implemented selecting a specific polarization or using a digital micromirror device. However, for amplitude modulation, the performance in terms of enhancement is expected to be

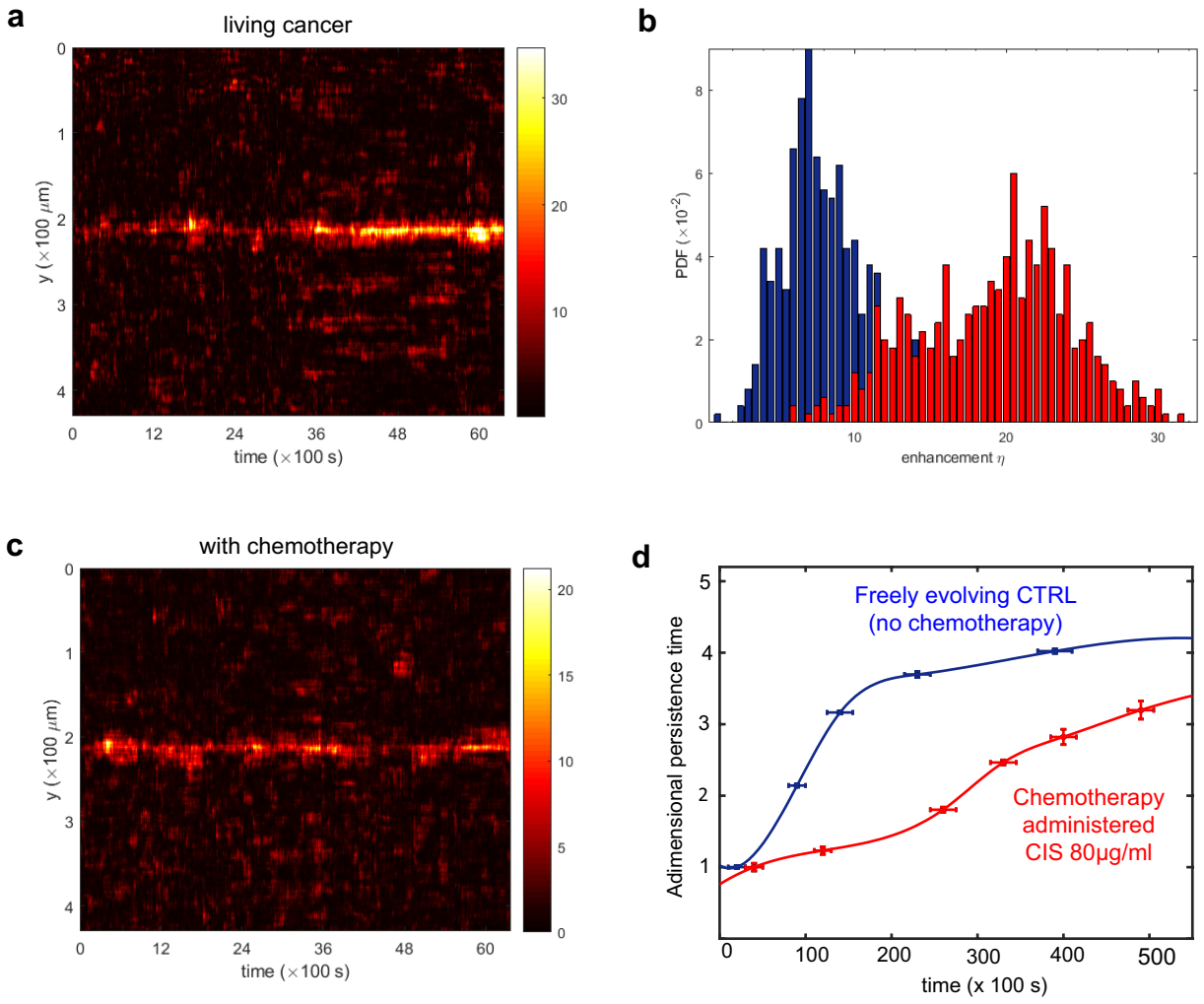

Supplementary Figure 7. Evolution of the random optical machine (ROM) output with the living tumor. (a) Output intensity (arb. units) detected as the cancer spheroid grows in time and (b) corresponding evolution of probability distribution function of the enhancement η (output efficiency). Initial stage: blue bars; final stage: red bars. (c) Detected target evolution under chemotherapy. (d) Persistence time as a function of the waiting time for untreated (blue dots) and cisplatin-treated (red dots) samples. Error bars are the statistical standard deviation over replicated experiments.

lower[12], a fact that in our case would reduce the sensitivity to the cellular dynamics.

SUPPLEMENTARY NOTE 6: SIGNAL-TO-NOISE RATIO BEFORE AND AFTER THE TRAINING

To demonstrate that training the network is an effective way to extract biophysical information from noise, we report here further measurement concerning the signal-to-noise ratio (SNR). Once optical transmission through the cancer spheroid is properly trained, the network output gives an optical signal that is extremely sensitive to internal variations of the multicellular structure. Supplementary Figure 8a (purple line) shows the intensity fluctuations in time when the laser is optimized to a single focus point. The measure quantifies the noise on the ROM output. Only minor intensity fluctuations of the target focus are present, these arising from noise sources in the experimental setup, including the thermal fluctuations of the sample. In the absence of the training, the intensity map is shown in Supplementary Figure 8, which does not change sensibly when we add the pump laser. On the contrary, the intensity map in the trained case changes radically when we turn on the pump (Supplementary Figure 8). The signal in Supplementary Figure 8 also allows excluding different effects such as cell dehydration, mechanical fluctuations of

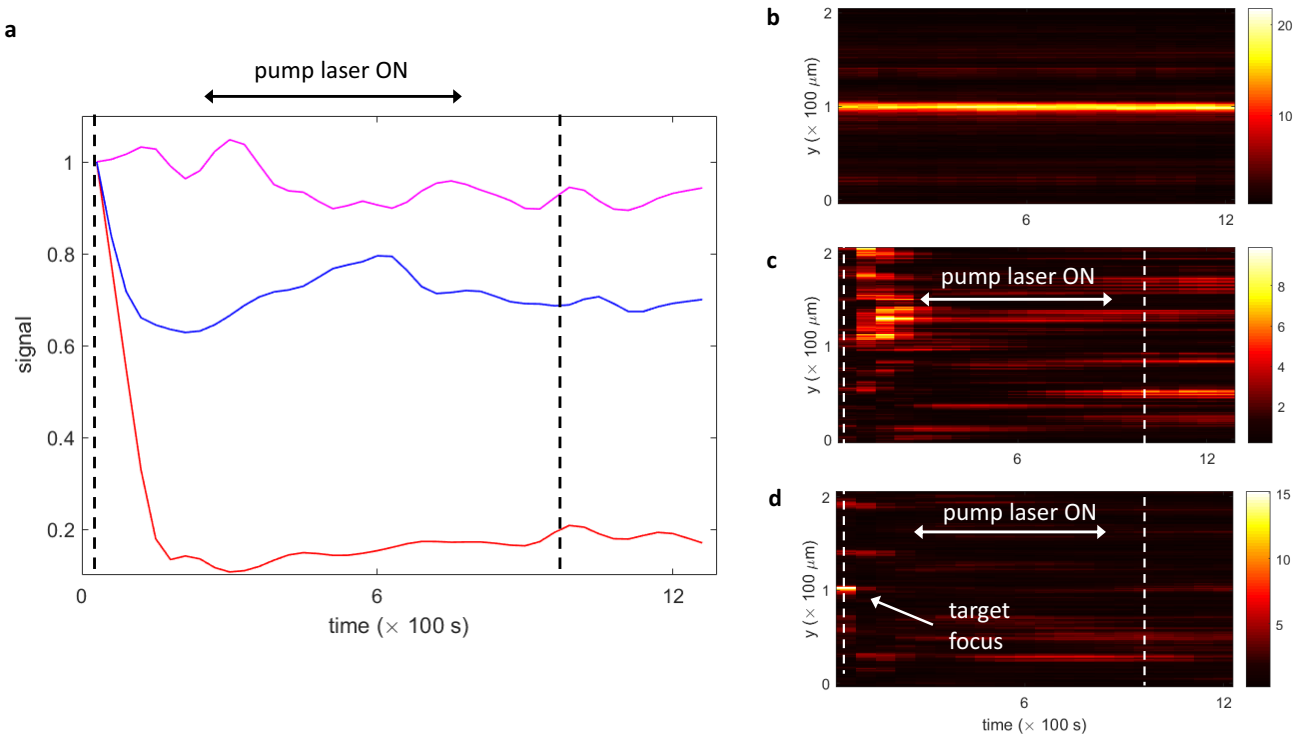

Supplementary Figure 8. Analysis of signal-to-noise ratio for the random optical machine (ROM), with and without training. a) evolution of the intensity fluctuations for: a single trained spot without infra red (IR) pump (purple), without training and with IR pump ON (blue). a single trained spot with IR pump ON (red). The vertical dashed lines indicate the turning on and off of the laser (b-d) Output spatial intensity (in the y-direction in the camera, measured in arb. units) for the three cases reported in panel a: b) a single trained spot without IR pump, c) without training and with IR pump ON. d) a single trained spot with IR pump ON. Dashed lines correspond to the turning on and off of the laser. Pump power: 1 W.

the biological assembly, laser fluctuations, etc. As shown in Supplementary Figure 8b), the trained output intensity in the absence of the pump IR laser and recurrent feedback is highly stable over a time scale of several minutes. On the contrary, as IR pumping is turned on, we find signal variations that are strongly correlated to the pump laser (Supplementary Figure 8d) The associated internal changes in the tumor spheroid morphology cannot be efficiently revealed collecting the transmitted light from a fixed untrained input wave. This statement is demonstrated by the experiments under IR pumping using untrained outputs (Supplementary Figure 8c) and compare the signal to noise ratio (SNR) characterizing both methods. As reported in Supplementary Figure 8a for $P = 1$ W, while the target signal presents a strong variation (red line), the variation of the output signal averaged over the output spatial modes for a fixed untrained input wave (blue line) is close to the measured noise level (magenta line). For the data set shown in Supplementary Figure 8, we find $SNR = 3.5$ and $SNR = 19.1$ respectively for the untrained and trained case. For the considered case we find an order of magnitude increase in the SNR ratio.

SUPPLEMENTARY NOTE 7: ABSENCE OF LASER-INDUCED DEHYDRATION AND RELATED EFFECTS

Optical imaging as in Fig. 5 of the main manuscript (Confocal Microscope, Nikon A1 MP) does not evidence any effect as dehydration or heating, as they would result in a change of nuclei size or distances. This occurs in all the experiments we report. The sample is in water solution. Hence no dehydration is expected. We remark that we do confocal microscopy in the presence of high power IR irradiation of the samples, which is the same condition in which we also use in the ROM. But optical imaging does not evidence any change. Previous studies [13] report that a sudden increase of temperature caused by laser irradiation can induce swelling and volume increase of isolated nuclei in Phosphate Buffer Solution but not of nuclei inside cells. We confirm these findings by aspect ratio and area measurements reported in Fig. 5 of the main manuscript. We also report in Supplementary Figure 9 further image analysis showing that correlation analysis of confocal images of spheroids (in Fig. 5, main manuscript) before and

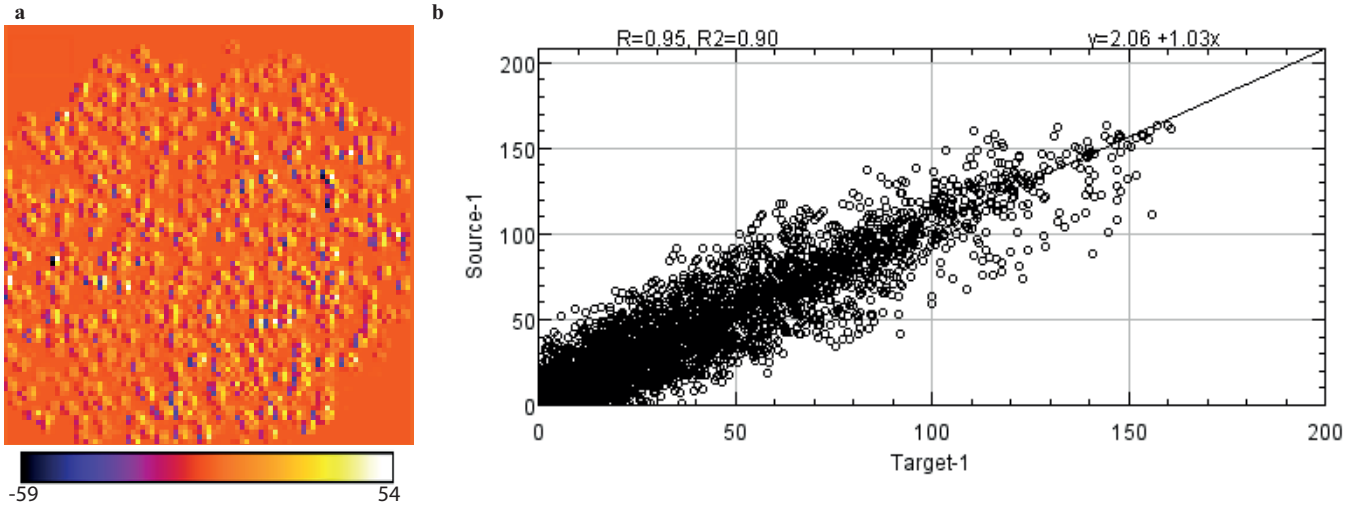

Supplementary Figure 9. Absence of dehydration and volume change due to infrared (IR) laser irradiation. Colocalization Analysis performed with Image CorrelationJ Plugin [14] using untreated spheroid as Source Image and the same spheroid after IR treatment as Target image. a. The Image CorrelationJ plugin generates a correlation map to visualize the local correlation at each local cell position (m_i, n_j). After the regression equation estimation (Panel b), for each local pixel area, the difference between the source and the target images is estimated according to: $d = s(m_i, n_j) - [at(m_i, n_j) + b]$ where d is the distance between the source image and the corresponding estimated value from the regression equation, $s(m_i, n_j)$ and $t(m_i, n_j)$ are the local values of the source and target images at position (m_i, n_j) respectively, and a and b are the constants of the regression equation [14]. b. Correlation between source and target image. Each dot represents a pixel area in each image, the line in the graph is the linear regression line. The correlation coefficient R is 0.95 and indicates high correlation between images.

during the IR treatment (after 30 s the turning on the pump) reveal no differences.

SUPPLEMENTARY REFERENCES

[1] All the references in this supplementary information refer to the Supplementary References.
[2] E. E. Economou, *Green's Functions in Quantum Physics* (Springer, Berlin, 2006).
[3] S. Rotter and S. Gigan, Reviews of Modern Physics **89**, 015005 (2017).
[4] A. Fleming, C. Conti, and A. Di Falco, arXiv:1809.07077 (2018).
[5] O. J. F. Martin, C. Girard, and A. Dereux, Physical Review Letters **74**, 526 (1995).
[6] S. Mittal, Neural Computing and Applications **32**, 1109 (2018).
[7] H. Jaeger and H. Haas, Science **304**, 78 (2004).
[8] C. Gallicchio, A. Micheli, and L. Pedrelli, Neural Netw. **108**, 33 (2018).
[9] C. Gallicchio, A. Micheli, and L. Pedrelli, Neurocomputing **268**, 87 (2017).
[10] G.-B. Huang, Q.-Y. Zhu, and C.-K. Siew, Neurocomputing **70**, 489 (2006).
[11] D. B. Conkey, A. N. Brown, A. M. Caravaca-Aguirre, and R. Piestun, Opt. Express **20**, 4840 (2012).
[12] D. Akbulut, T. J. Huisman, E. G. van Putten, W. L. Vos, and A. P. Mosk, Opt. Express **19**, 4017 (2011).
[13] C. J. Chan, W. Li, G. Cojoc, and J. Guck, Biophysical Journal **112**, 1063 (2017).
[14] G. Chinga and K. Syverud, Nordic Pulp and Paper Research Journal **22**, 441 (2007).